Double Cross-Linked Hydrogel for Intra-articular Injection as Modality for Macrophages Metabolic Reprogramming and Therapy of Rheumatoid Arthritis

Yutong Song, Valentin A. Milichko, Ziqiao Ding, Wen Li, Bei Kang, Yunsheng Dou, Sona Krizkova, Zbynek Heger, and Nan Li**

Rheumatoid arthritis (RA) is a chronic inflammatory disease associated with abnormalities of the immune system. Recently, the metabolic disorder of immune cells and imbalance within their microenvironment are delineated as key factors triggering the initiation and progression of RA. Therefore, in the present study, injectable hydrogel (hereinafter referred to as siHPTs@ZA hydrogel) assembled through Zn^{2+}-mediated ionic cross-linking of alginate further cross-linked with hyperbranched poly(β-amino ester) loaded with TNF-α siRNA. The resulting siHPTs@ZA hydrogel is successfully employed to induce metabolic reprogramming of macrophages toward regulating the ratio of M1/M2 polarization. In the hypoxic microenvironment, administration led to downregulation of the *GLUT1* expression consequently suppressing pro-inflammatory M1 macrophages relying primarily on glycolysis. In addition, exposure to an acidic environment triggered the degradation of siHPTs@ZA hydrogel resulting in the release of Zn^{2+} that activated expression of PPARγ accelerating fatty acid oxidation, subsequently inducing anti-inflammatory M2 macrophage polarization. Taken together, under a hypoxic microenvironment, the presented injectable hydrogel is able to induce reprogramming of immunometabolism, thus being a promising platform for next-generation, highly efficient treatment of RA.

1. Introduction

Rheumatoid arthritis (RA) is a chronic, inflammatory autoimmune disease that causes progressive joint destruction, disability, and substantially reduced quality of life.[1,2] Currently, approved modalities for RA therapy involve traditional disease-modifying antirheumatic drugs, synovectomy, and nonpharmacological interventions, such as exercise, diet, and others.[3,4] During RA progression, the synovium is the primary tissue, in which pathogenic events such as inflammation, oxidative stress, and hypoxia initiate joint destruction.[5] Together, these phenomena induce a unique hypoxic/inflammatory RA microenvironment, leading to dysfunction and imbalance of immune cell homeostasis, resulting in markedly higher needs for energy supplies required for metabolic reprogramming.[6,7]

It has been shown that the activation and function of macrophages are influenced by altered cellular metabolism, involved in the pathogenesis of RA, subsequently affecting the immune microenvironment as well as the production and differentiation of immune cells.[7,8] In addition, a higher ratio of M1-to-M2 macrophages in RA promotes the production of proinflammatory cytokines such as interleukin-1β (IL-β) and tumor necrosis factor-α (TNF-α), further worsening the progression of RA. Therefore, it could be expected that targeted intervention/regulation of relevant immune metabolism pathways might be a promising strategy for RA therapy.

Y. Song, Z. Ding, W. Li, B. Kang, Y. Dou, N. Li
Tianjin Key Laboratory of Drug Delivery & High-Efficiency
School of Pharmaceutical Science and Technology
Faculty of Medicine
Tianjin University
Tianjin 300072, China
E-mail: linan1985@tju.edu.cn

The ORCID identification number(s) for the author(s) of this article can be found under https://doi.org/10.1002/adfm.202502880

DOI: 10.1002/adfm.202502880

V. A. Milichko
School of Physics and Engineering
ITMO University
St. Petersburg 197101, Russia

S. Krizkova, Z. Heger
Department of Chemistry and Biochemistry
Mendel University in Brno
Brno 61300, Czech Republic
E-mail: zbynek.heger@mendelu.cz

Z. Heger
Center of Advanced Innovation Technologies
Faculty of Materials Science and Technology
VSB – Technical University of Ostrava
Ostrava 70800, Czech Republic

Glucose and lipid metabolisms are the main metabolic pathways differentiating phenotypes of immune cells. It has been shown that classically activated macrophages prefer glycolysis; however, during alternative macrophage activation, their metabolism tends to utilize fatty acid oxidation (FAO).[9] Thus, it is not surprising that several studies have discussed metabolic dysregulation as a possible therapeutic target for specific pathologies including RA,[10,11] and it is therefore plausible that deregulated metabolism may play a crucial role in the pathological action of macrophages. Glucose metabolism is one of the primary metabolic pathways, including glycolysis, aerobic oxidation, and pentose phosphate metabolism, fundamental for a variety of physiological processes.[12] Thereby reprogramming toward blockage of glycolysis and inhibition of M1 polarization leads to downregulation of cytokines production.[13] In the RA microenvironment, hypoxic conditions activate hypoxia-inducible factor-1α (HIF-1α) expression. Noteworthy, HIF-1α also participates in driving M1 polarization by upregulating the expression of glycolysis-related glucose transporters GLUT1/GLUT3 particularly in chondrocytes, and several glycolytic enzymes in cartilage.[14–16] In particular, GLUT1 is a critical inducible factor for glucose metabolism to fuel the glycolytic pathway.[17–19] Therefore, the therapeutic strategy for macrophage metabolic reprogramming must be designed to first inhibit this part of glycolysis to efficiently stop ATP production.

As stated above, lipid metabolism, another crucial cellular pathway of energy production, stimulates the activation of M2 macrophages.[20] In sharp contrast with the metabolic characteristics of inflammatory macrophages, hypoxia impairs anti-inflammatory macrophages' FAO pathway by downregulating FAO-driving enzymes.[21–23] Thus, promoting macrophage fatty acid catabolism by FAO could attenuate inflammation associated with metabolic disorders.[15] Peroxisome proliferator-activated receptor (PPAR) is a pivotal factor for the transport and catabolism of fatty acids. PPAR also plays a metabolic immunomodulatory role in immune cells.[24] Among them, PPARγ, primes macrophages into M2 phenotype and is a ligand-activated nuclear receptor controlling FAO pathway and the inflammatory response of M2 macrophages.[25,26] Taken together, based on glucose and lipid metabolism as the primary activation types of immune cells, inhibiting glucose metabolism while stimulating lipid metabolism seems to be a logical approach for RA treatment.

Currently, intra-articular injection is one of the preferred administration routes in RA therapy. This is due to increased bioavailability and reduced toxicity compared to systemic administration.[27,28] Injectable biomaterials for intra-articular administration thus represent a highly promising approach to developing next-generation RA therapeutic modalities.[29] This statement is further supported by the fact that anti-RA drugs are characterized by short half-lives and rapid clearance from joints.[30] Injectable hydrogels possessing 3D, cross-linked architecture, act as drug reservoirs, thereby increasing the residence time of the drug and allowing for sustained drug release.[31]

One possible approach is to formulate therapeutic agents loaded in hydrogel nano/microspheres. These have emerged as a novel and efficient drug delivery system particularly due to their excellent biocompatibility, modular combinability, and modifiability.[32] Alginates are natural anionic polymers that are nontoxic, cheap, and capable of effective control of drug release due to their pH sensitivity.[33–35] The most common strategy of alginate hydrogel formation is ionic crosslinking, exploiting divalent Zn^{2+} as an ionic chelating agent to form an "egg-box" structure.[36,37] After the intra-articular injection, Zn^{2+}-cross-linked alginate-based hydrogels degrade in an inflamed acidic RA microenvironment and release zinc ions.[33–35] However, single alginate hydrogels exhibit large porosity, which contributes to rapid dissolution and instability. Therefore, the production of double cross-linked hydrogel networks is crucial to improving the biophysical properties of alginate-based hydrogel nano/microspheres.[38]

Hence, in this work, a double network alginate hydrogel was formulated through Zn^{2+}-mediated cross-linking of alginate further cross-linked with hyperbranched poly(β-amino esters) (HB-PBAEs) loaded with TNF-α siRNA (hereinafter referred to as siHPTs). The resulting structure (siHPTs@ZA hydrogel) was employed to induce the metabolic reprogramming of macrophages for RA therapy (depicted in **Scheme 1**). We showed that upon intra-articular administration of siHPTs@ZA hydrogel, the alginate network degrades followed by the release of zinc ions and siHPTs. Consequently, the proton sponge effect HB-PBAE promotes endolysosomal escape of TNF-α siRNA to the cytoplasm.[39,40] This leads to a down-regulation of proinflammatory TNF-α over-produced within the RA microenvironment and subsequent inhibition of chronic inflammation via dampening the energy supplies for M1 macrophages. Furthermore, TNF-α down-regulation suppresses the GLUT1 expression and inhibits glycolysis. In addition, released zinc ions act as PPARγ agonists affecting the transcriptional activity of PPARγ while boosting the FAO pathway of anti-inflammatory macrophages. Taken together, siHPTs@ZA hydrogel was found to be able to switch macrophage metabolism from M1-glycolytic to M2-lipid-based. Thus, it can be considered as a new generation of therapeutic modality for RA treatment utilizing macrophage immunoregulation.

2. Results and Discussion

2.1. Design and Characterization of siHPTs@ZA Nanospheres

The dual cross-linked nanospheres were constructed in a microfluidic chip by rapid mixing of HB-PBAE loaded with TNF-α siRNA, alginate, and Zn^{2+} (**Figure 1**A). As demonstrated by transmission electron microscopy (TEM), the formulation produced homogeneous spherical particles with an average diameter of ≈200 nm as confirmed by dynamic light scattering (DLS) (Figure 1B; Figure S1, Supporting Information). To achieve this, we first synthesized cationic HB-PBAE via Michael addition between poly(ethylene glycol) diacrylate (PEGDA) and cystamine (Figure S2, Supporting Information). ^1H-nuclear magnetic resonance (^1H-NMR) spectrum was recorded for both, PEGDA and cystamine (Figure S3, Supporting Information), and also for HB-PBAE verifying its successful synthesis. The characteristic proton peaks at 3.4 and 3.6 ppm attributed to the tertiary hydrogen group and the acrylate protons on terminal double bond at 5.7 and 6.5 ppm are shown in Figure 1C. In addition, the molecular weight of HB-PBAE was analyzed using gel permeation

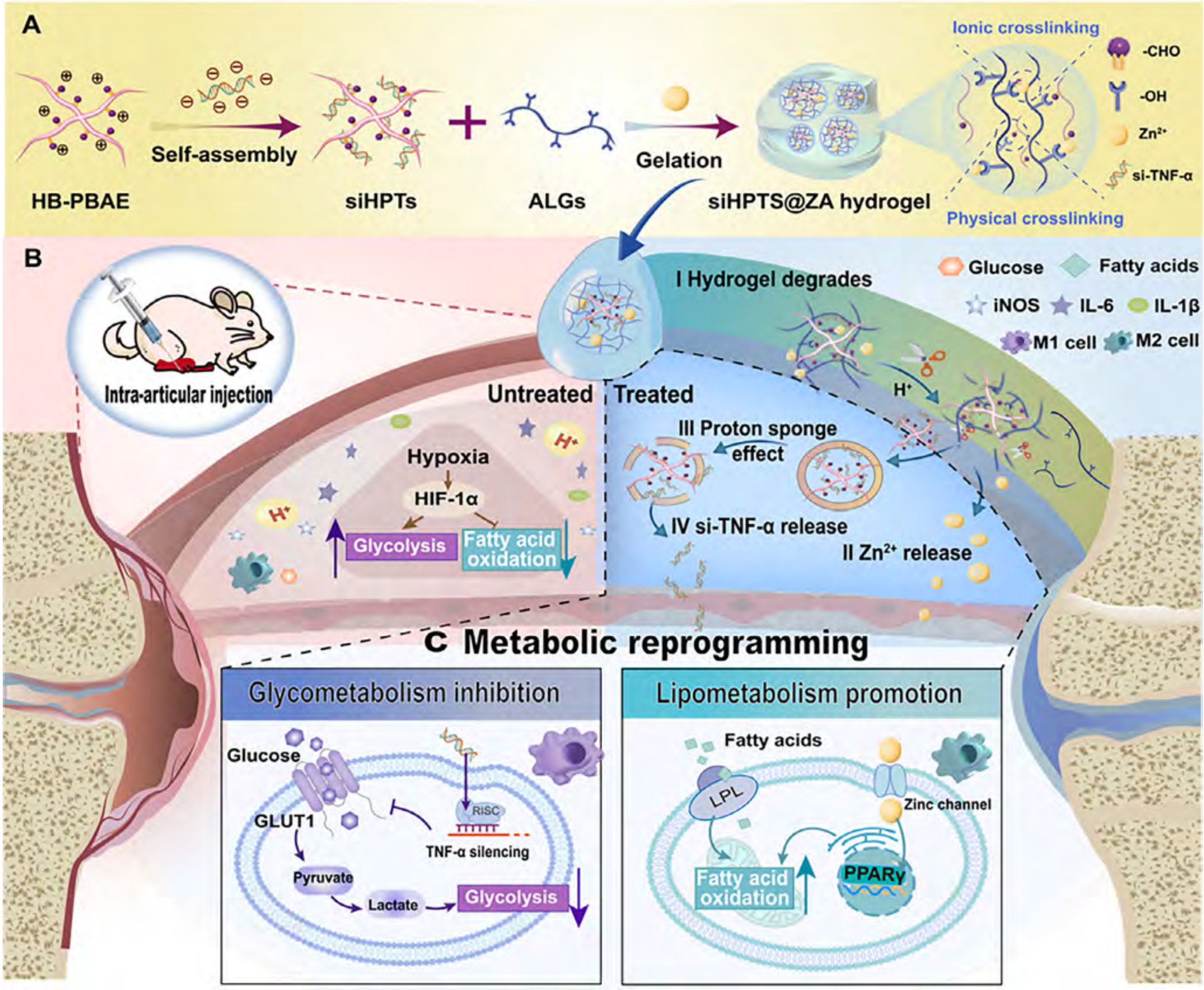

Scheme 1. A) Schematic depiction of the preparation of siHPTs@ZA hydrogel formed by a double cross-linked network for direct intra-articular administration. B) Fate of siHPTs@ZA hydrogel in RA microenvironment after intra-articular injection. C) Mechanism of metabolic reprogramming from glycolysis to lipid metabolism.

chromatography (GPC) and was found to be ≈8.5 kDa (Figure 1D). The elemental composition of HB-PBAE is shown in Figure S4 (Supporting Information). In clinical applications, the use of siRNA effectors is markedly hampered due to their low stability and inability to cross cellular membranes and escape endolysosomal compartments.[41,42] Thus, in our study, positively charged HB-PBAE was employed for siRNA loading via electrostatic adsorption. After the interaction, HB-PBAE and siRNA self-assemble into siHPTs, and the assembly process can be easily monitored through surface zeta potential analysis (Figure 1E). To further test the encapsulation efficiency of TNF-*α* siRNA, an agarose gel electrophoresis was carried out. As shown in Figure 1F, large amounts of free siRNA were observable when the weight ratio was 0.5:1 or 1:1, while there was no obvious difference in the amount of free TNF-*α* siRNA for ratios of 5:1 to 10:1. This indicated that at ratios of >20:1, HB-PBAE was able to encapsulate the majority of siRNA. Considering this, for follow-up experiments, 20:1 was chosen as the optimal weight ratio of HB-PBAE: siRNA.

Alginate is composed of the repetitive *β*-D-mannuronic acid (M units) and *α*-L-guluronic acid (G units) linked by glycosidic bond. Its inner carboxyl groups are easily chelated with divalent cations to form the "egg-box" structure.[37] Accordingly, we proceeded to circular dichroism (CD), which confirmed the spatial structure of alginate (positive peak at ≈200 nm corresponding to the M unit, and negative peak at ≈215 nm corresponding to the G unit). Thus, it can be concluded that the Zn^{2+}-mediated cross-linking did not have any deleterious effects on alginate structure. In addition, CD spectra revealed that zinc-alginate (ZA) gels exhibited a peak at ≈190 nm (Figure 1G). To formulate the best possible alginate nanospheres, different concentrations of zinc ions were tested (Figure S5, Supporting Information). Since the use of 0.25% of ZA mixed with siHPTs in a microfluidic chip reproducibly gained the nanospheres with size ≈255 nm with the

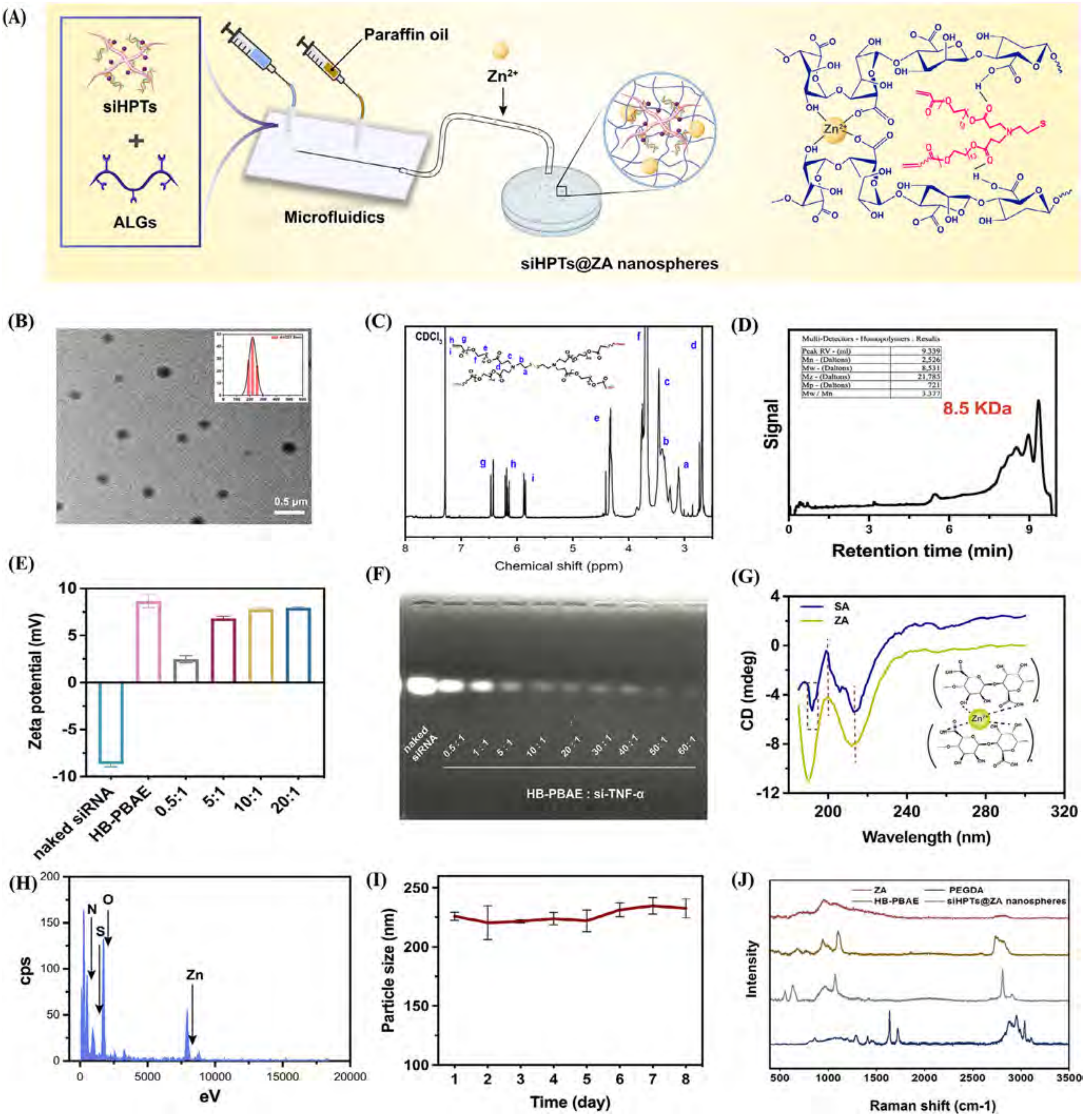

Multi-Detectors - Homopolymers : Results

Peak RV - (ml)	9.339
Mn - (Daltons)	2,526
Mw - (Daltons)	8,531
Mz - (Daltons)	21,785
Mp - (Daltons)	721
Mw / Mn	3.377

Figure 1. Preparation and characterization of siHPTs@ZA nanospheres. A) Schematic illustration of the synthesis of siHPTs@ZA nanospheres through microfluidics-mediated rapid mixing. B) TEM image of siHPTs@ZA nanospheres (scale bar, 0.5 μm). Inserted is the DLS size histogram of siHPTs @ZA nanospheres. C) ^{1}H-NMR spectrum of HB-PBAE. D) GPC of HB-PBAE. E) Zeta potential values of naked TNF-*α* siRNA, HB-PBAE, and HB-PBAE loaded with TNF-*α* siRNA at various weight ratios (0.5:1–20:1). The data are expressed as mean ± SD (*n* = 3) represented by error bars. F) Agarose gel retardation assay of TNF-*α* siRNA after elution from siHPTs assembly formulated with various weight ratios of HB-PBAE and TNF-*α* siRNA. G) CD spectra of alginate-Zn^{2+} gels (ZA) and sodium alginate (SA). H) EDS spectrum of the siHPTs@ZA nanospheres. I) Stability of siHPTs@ZA nanospheres in PBS at 37 °C for 8 days. The data are expressed as mean ± SD (*n* = 3) represented by error bars. J) Raman spectra of PEGDA, HB-PBAE, ZA, and siHPTs @ZA nanospheres.

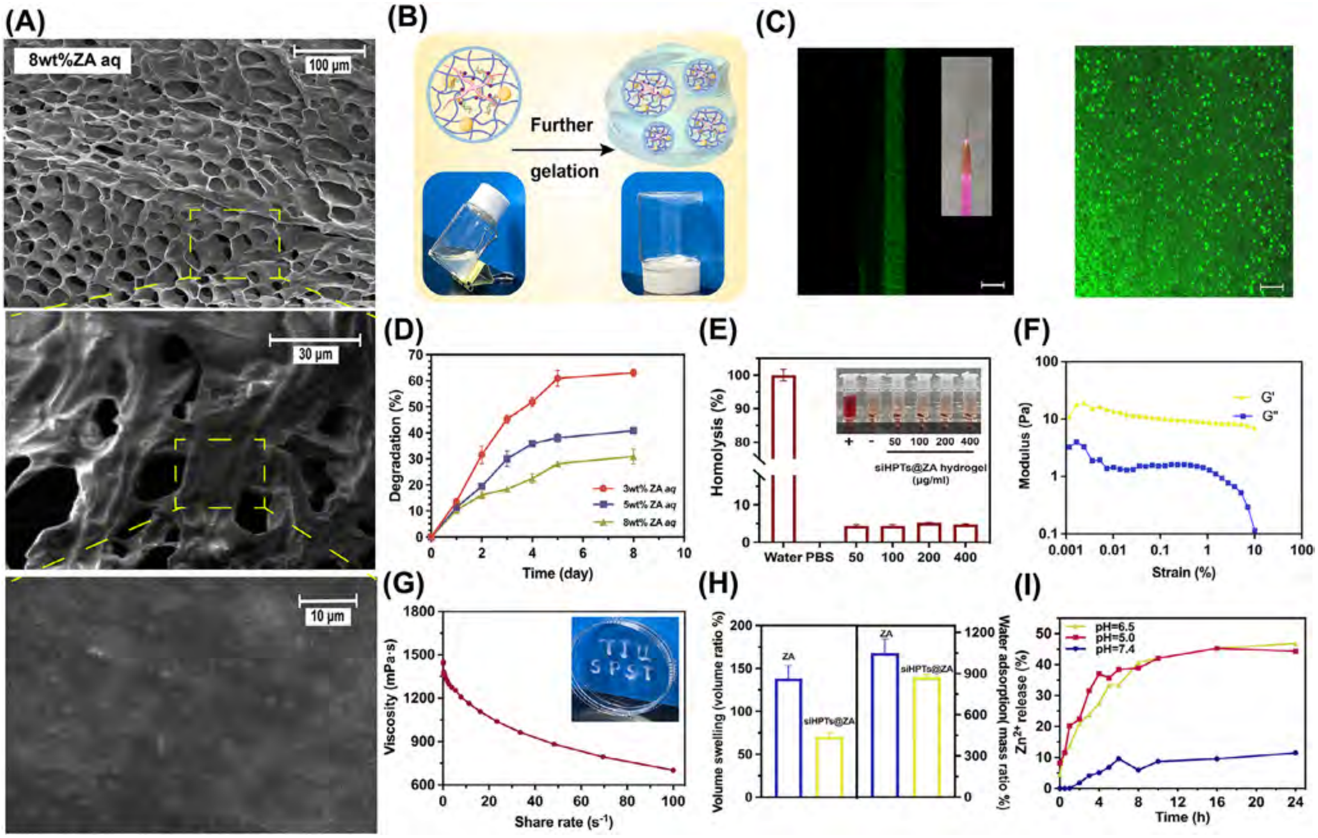

Figure 2. Formulation and characterization of injectable siHPTs@ZA hydrogel. A) SEM micrographs of siHPTs@ZA hydrogel gelated using 8% wt ZA aqueous solution (scale bars, 100, 30, and 10 μm) B) Depiction of sol-gel transition of siHPTs@ZA hydrogel to promote further gelation. C) Injectability of hydrogel using a 1 mm syringe and distribution of FITC-labelled siHPTs@ZA nanospheres observed by confocal microscopy. D) Evaluation of degradation of siHPTs@ZA hydrogels formulated using differing concentrations of ZA aqueous solution. The data are expressed as mean ± SD ($n = 3$) represented by error bars. E) Hemolytic properties of siHPTs@ZA hydrogel. The data are expressed as mean ± SD ($n = 6$) represented by error bars. F) Rheological analysis of siHPTs@ZA hydrogel in strain sweep experiment. G) Viscosity of siHPTs@ZA hydrogel. H) siHPTs@ZA hydrogel mass/volume degree of swelling ratio. The data are expressed as mean ± SD ($n = 3$) represented by error bars. I) In vitro release kinetics of Zn^{2+} from siHPTs@ZA hydrogel during incubation in buffers differing in pH (7.4, 6.5, and 5.0).

highest homogeneity (lowest PDI), this formulation was used in subsequent experiments.

Further, energy dispersive spectroscopy (EDS) confirmed the presence of Zn, N, O, and S in siHPTs@ZA nanospheres (Figure 1H). DLS further confirmed that siHPTs@ZA nanospheres exhibited remarkable stability with no detectable change in size during 8 days of incubation at 37 °C (Figure 1I). UV–Vis analyses of siHPTs@ZA nanospheres revealed a strong absorption of nanospheres at 510 nm, which verified the presence of the conjugated double bonds and carbon-oxygen double bonds in alginate intermolecular interactions (Figure S6, Supporting Information). Similarly, the alginate structure was confirmed by Fourier-transform infrared (FT-IR) spectroscopy demonstrating the hydroxyl group at approximately 3000 cm^{-1} and the carboxyl group at 1410 cm^{-1} (Figure S7, Supporting Information). Moreover, Raman spectroscopy revealed a disulfide bond peak at 520 cm^{-1} corroborating the inherent disulfide-containing structure of HB-PBAE. After mixing the ZA and the siHPTs, the final siHPTs@ZA nanospheres exhibited an alginate peak at 1000–1200, and a peak of 3000 cm^{-1} originating from PEGDA presence (Figure 1J).

2.2. Formulation of Injectable siHPTs@ZA Hydrogel

The injectable hydrogel formed from siHPTs@ZA nanospheres was prepared by freeze-drying of siHPTs@ZA nanospheres, which were subsequently gelated by letting them stand in an aqueous solution containing dissolved nanospheres (ZA) without siHPTs until the solution fully permeated into the cross-linked network.[43] To optimize the siHPTs@ZA hydrogel architecture, three different concentrations of dissolved ZA solution were tested and the morphology of lyophilized hydrogels was characterized by scanning electron microscopy (SEM) (**Figure 2**A; Figure S8, Supporting Information). SEM micrographs demonstrated that 8% wt siHPTs@ZA hydrogels formed a highly uniform porous network architecture. The network structure of hydrogel fibers became gradually denser because of the molecular (chain) interaction enhancement due to the increasing amount of ZA. Further magnification of the porous structure revealed plenty of siHPTs@ZA nanospheres attached to the surface (Figure 2A). In the next step, sol-gel phase transition was carried out (Figure 2B) to promote further cross-linking and form hydrogel. As shown in Figure 2C, the hydrogel exhibited good injectability, allowing for continuous injection through 1 mm syringe with relatively low extrusion force. Additionally, by labeling the siHPTs@ZA nanospheres with fluorescein isothiocyanate (FITC) and observing the microstructure of the extruded hydrogel under confocal laser scanning microscope (CLSM), it was also observed that it contained a large amount of siHPTs@ZA nanospheres, resembling structures observable under SEM (**Figures** S9 and S10, Supporting Information). Noteworthy, it was observed that the nanospheres were not tightly packed but rather loosely bound, with some degree of flow and sliding freedom. This further supports that the siHPTs@ZA hydrogel exhibits good biomechanical properties, meeting the prerequisites for injectable formulations.

It must be noted that in general, alginate hydrogels possess several advantages over some of the current chemical gel materials, including complete non-toxicity, elasticity, and good biodegradability.[44] The stability of siHPTs@ZA hydrogels was further explored and it was found that for siHPTs@ZA hydrogel formulated using 8% wt ZA, ≈40% degradation occurred after 8 days of incubation in PBS (Figure 2D). The 8% concentration allows this hydrogel to be degradable while also increasing the retention time of more effective ingredients. In addition, siHPTs@ZA hydrogel exhibited excellent hemocompatibility (hemolysis ˂5.0%) (Figure 2E).

To further understand the biomechanical properties of the hydrogel, we performed a rheological analysis of viscoelasticity, which is essential to describe the behavior of a hydrogel following injection.[45] It was found that the storage modulus (G’) was higher than the loss modulus (G″), confirming siHPTs@ZA hydrogel solid gelatinous property (Figure 2F). Additionally, its viscosity decreased progressively as shear rates increased during extrusion, indicating that hydrogel displayed the classic shear-thinning behavior. After light compression, siHPTs@ZA hydrogel possessed good injectability (Figure 2G). Swelling of hydrogels is crucial for substance exchange when used as injectable scaffolds for drug delivery. Figure 2H illustrates that hydrogel exhibited good swelling capacity. The swelling increased rapidly to the equilibrium and an extremely high swelling mass ratio of over 1000% for ZA and 800% for siHPTs@ZA hydrogel was observed. Similarly, the swelling volume ratio of over 100% for ZA and 50% for siHPTs@ZA hydrogel was found. This could be explained by the architecture of hydrogel, in which the internal -COO^-- not only hydrated with the water molecules, but also stretched the polymer chain through the water. Further, the pH responsiveness of hydrogel was investigated by quantifying zinc release kinetics during hydrogel incubation in buffers differing in pH. As shown in Figure 2I, exposure to an acidic environment triggered sustained release of zinc from siHPTs@ZA hydrogel (≈50% of zinc ions were released after 1 day in both acidic conditions), while in neutral buffer, only a neglectable zinc release was found, highlighting excellent pH responsiveness of the hydrogel.

2.3. Evaluation of Biological Activity of siHPTs@ZA Hydrogel In Vitro

Local delivery of siRNA for which siHPTs@ZA hydrogel was formulated, may be employed to overcome severe limitations associated with enzymatic degradation and rapid clearance of siRNA after systemic administration.[41,42] However, to achieve RNA interference, siRNA must be released from a delivery vehicle followed by endosomal escape. Therefore, next, we investigated the uptake and intracellular fate of FITC-labeled siHPTs@ZA hydrogel in RAW264.7 macrophages. As demonstrated in **Figure** 3A, at examined time points (0, 2, 4, 8, and 12 h), the fluorescence signal of siHPTs@ZA hydrogel reached its maximum between 2 and 4 h, verifying successful rapid internalization. Moreover, it was found that siHPTs@ZA hydrogel exhibited an excellent endosomal escape ability, suggesting subsequent functionality of siRNA. Subsequently, we evaluated the cytotoxicity of siHPTs@ZA hydrogel in different RAW264.7 macrophage phenotypes (M0, M1, and M2) (Figure 3B). Irrespective of phenotype, there was no observable cytotoxicity, confirming excellent biocompatibility of siHPTs@ZA hydrogel in vitro. In addition, to understand the cytotoxic properties of individual components of siHPTs@ZA hydrogel, RAW264.7 macrophages were treated with ZA, Alg-siHPTs, siHPTs, and siHPTs@ZA hydrogel. The obtained data corroborated the biocompatibility of the results presented in Figure S11 (Supporting Information).

2.4. Evaluation of Transfection Efficiency in RAW264.7 Macrophages In Vitro

To explore the transfection efficiency, we further evaluated various weight ratios of ZA and siHPTs used for the formulation of siHPTs@ZA hydrogels. A schematic depiction of the expected knock-down, based on the uptake/intracellular fate results presented above is shown in Figure 3C. In the first experiment, it was found that changing the mass ratios of ZA and siHPTs did not exhibit any significant effects on RAW264.7 macrophages (Figure 3D) and that commercial transfection agent Lipofectamine 2000 (Lipo2000) displayed slightly higher cytotoxicity compared to siHPTs@ZA hydrogels. Further, the intracellular distribution of fluorescein amidite (FAM)-labeled siRNA was explored after transfection with different types of siHPTs@ZA hydrogels and Lipo2000. Figure 3E demonstrates that the highest fluorescence intensity was found Lipo2000 followed by siHPTs@ZA hydrogel formulated with 1:8 ZA and siHPTs. This was further corroborated by quantification of FAM fluorescence intensity (Figure 3F). The data revealed that the siRNA signal is rather smoothly distributed across the cytoplasm with minimal granularity, confirming the successful accumulation of siRNA in the cytoplasm, which is a crucial prerequisite for any follow-up experiments. Consequently, we further used two representative ratios of ZA and siHPTs (1:4 and 1:8) and assessed the TNF-α siRNA knock-down efficiency. As shown in Western blot and quantified relative expression of TNF-α (Figure 3G,H), siHPTs@ZA hydrogel formulated using a 1:8 weight ratio of ZA and siHPTs reached comparable knock-down as Lipo2000, while 1:4 weight ratio siHPTs@ZA hydrogel exhibited only insignificant TNF-α down-regulation, which is in line with distribution experiments presented in Figure 3E,F. Since siRNA employs the RISC complex to degrade target mRNA,[46] we decided to confirm the obtained data by quantitative polymerase chain reaction (qPCR). Indeed, qPCR data in Figure 3I confirmed the trends in TNF-α knock-down efficiency as observed at the mRNA expression level, consistently with the previous immunofluorescence

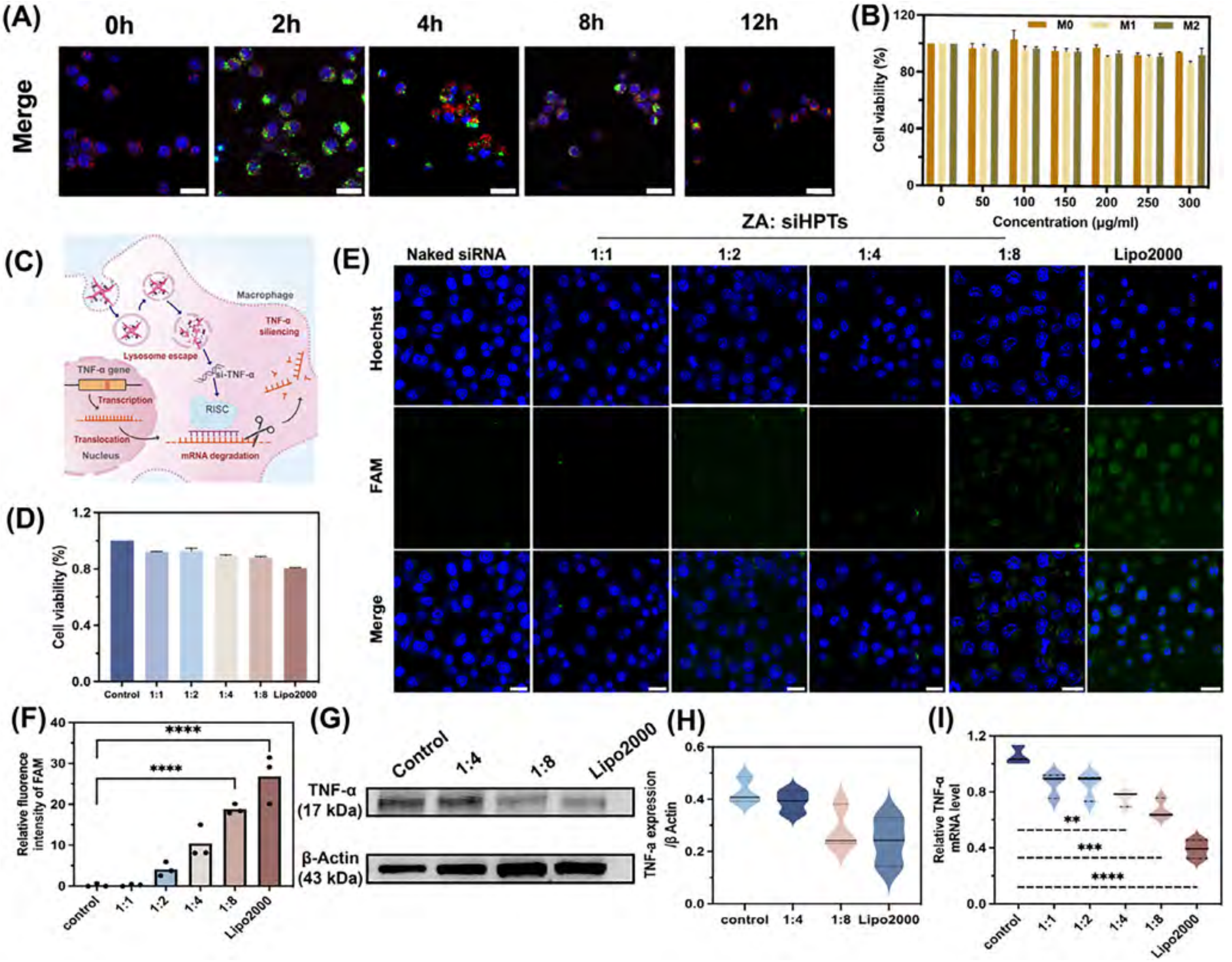

Figure 3. A) Confocal micrographs of cellular uptake of FITC-labeled siHPTs@ZA hydrogel (green) by RAW264.7 macrophages. Nuclei were counterstained with Hoechst33342 (blue), and lysosomes were stained with LysoTracker (red). Scale bar, 20 μm. B) Viability of RAW264.7 macrophages administered with siHPTs@ZA hydrogel for 24 h. The data are expressed as mean ± SD ($n = 3$) represented by error bars. C) Schematic illustration of siHPTs@ZA hydrogel-mediated transfection and subsequent inhibition of TNF-α expression in macrophages. D) Viability of RAW264.7 macrophages treated with naked TNF-α siRNA (control) and siHPTs@ZA hydrogels formulated with varying weight ratios of siHPTs and ZA. As a positive control, TNF-α siRNA transfected using the commercial transfection agent Lipo2000 was used. E) Confocal micrographs showing the intracellular distribution of FAM-labeled siRNA after transfection of RAW264.7 macrophages with various types of siHPTs@ZA hydrogels (ZA:siHPTs ratio) and Lipo2000, respectively. Blue, nuclei; green, FAM-labeled siRNA. Scale bar, 20 μm. F) Quantification of fluorescence intensity of FAM-labeled siRNA based on confocal micrographs shown in (E). The data are expressed as mean ± SD ($n = 3$) represented by error bars. G) Western blot and H) relative quantification of TNF-α expression in RAW264.7 macrophages treated with siHPTs@ZA hydrogels and Lipo2000. β-actin, loading control. I) qPCR analysis of TNF-α-encoding mRNA. In immunoblots and qPCR experiments, naked TNF-α siRNA served as control. The data are expressed as mean ± SD ($n = 3$), $^{**}p < 0.01$, $^{***}p < 0.001$, $^{****}p < 0.0001$.

staining. Taken together, the results underpinned that 1:8 ratio of ZA and siHPTs NPs used to formulate siHPTs@ZA hydrogel was the best choice for subsequent experiments.

2.5. Inhibition of Glycolytic Metabolism and M1 Polarization

Based on the hypoxia microenvironment of RA, it has been demonstrated that lipopolysaccharide/interferon γ (LPS/IFNγ)-activated macrophages tend to carry out cellular metabolism through the aerobic glycolysis pathway. Furthermore, anti-TNF-α-based therapies have been found to downregulate GLUT1 expression, which is a rate-limiting enzyme in glycolytic metabolism.[47–50] Considering these findings, we next investigated how pro-inflammatory M1 macrophage polarization associates with glycolysis (**Figure** 4A). The scheme shows that glucose is transported by GLUT1 and then converted into lactate, leading to the accumulation of lactate in the joints, and causing pain. In line with this, we confirmed that the LPS/IFNγ-induced macrophages displayed a remarkable increase in pyruvate production (+10.8%) and glucose consumption (+18.3%) compared to the control non-induced macrophages. After treatment

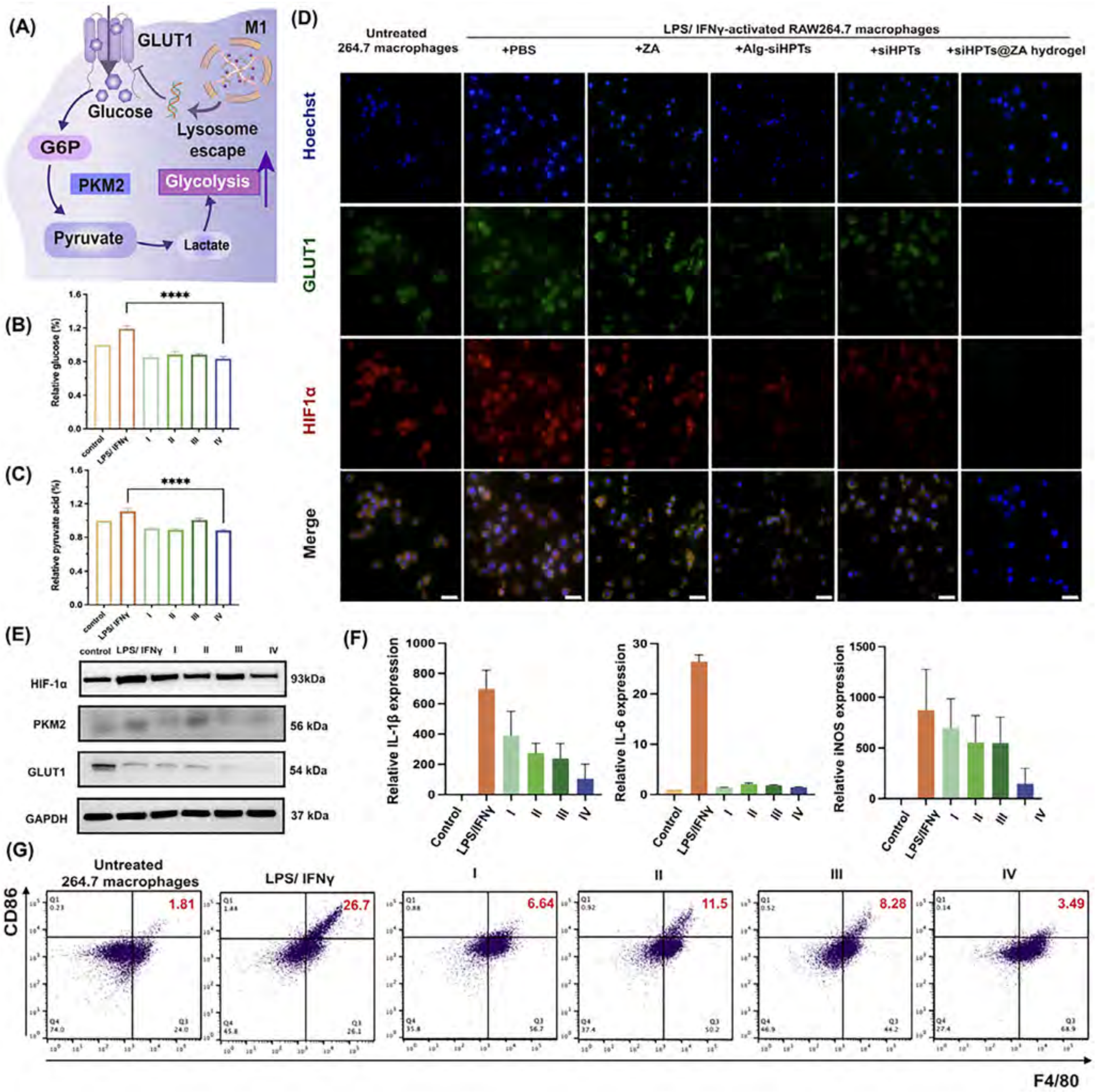

Figure 4. Inhibition of glycolytic metabolism and M1 polarization of RAW264.7 macrophages. A) Schematic depiction of the inhibition of glycolysis pathway and subsequent blocking of M1 polarization. B) Glucose consumption and C) pyruvate production in RAW264.7 macrophages. The data are expressed as mean ± SD ($n = 3$) represented by error bars. D) Representative immunofluorescence micrographs of GLUT1 and HIF-1α expression in RAW264.7 macrophages (scale bar, 20 µm). E) Western blots of HIF-1α, GLUT1, and PKM2 expression in RAW264.7 macrophages. GAPDH, loading control. F) Relative expression of M1 macrophage markers detected in RAW264.7 macrophages. The data are expressed as mean ± SD ($n = 3$) represented by error bars. G) Flow cytometry dotplots of CD86 expression in RAW264.7 macrophages. Groups: I: ZA, II: Alg-siHPTs, III: siHPTs, IV: siHPTs@ZA hydrogel. The data are expressed as mean ± SD ($n = 3$), $^{****}p < 0.0001$.

with siHPTs@ZA hydrogel, both pyruvate and glucose amounts dropped to −11.6% and −14.0%, respectively (Figure 4B,C). The hypoxic microenvironment of RA is characterized by HIF-1α expression increase in the synovial membrane, which directly stimulates cell metabolism through anaerobic glycolysis as an adaptation to the hypoxic environment.[51] Hence, we further investigated how HIF-1α participates in the regulation of M1 polarization by inducing the expression of GLUT1. As shown in Figure 4D and Figure S12 (Supporting Information), LPS/IFNγ-activated macrophages displayed stronger HIF-1α expression compared to untreated RAW246.7 macrophages. Further, in LPS/IFNγ-activated macrophages, treatment with siHPTs@ZA hydrogel, resulted in nearly complete diminishing of both, HIF-1α and GLUT1 signals. Thus, it can be stated that siHPTs@ZA hydrogel successfully inhibits hypoxic signaling and glycolytic metabolism of M1 macrophages in vitro. To corroborate this finding, we also carried out Western blotting, which confirmed that siHPTs@ZA hydrogel (group IV) down-regulated HIF-1α and GLUT1 expression (Figure 4E; **Figures** S13 and S14, Supporting Information), while also down-regulating expression of pyruvate kinase M2 (PKM2), which is an important glycolytic enzyme.[52]

In a consequent effort to delineate the pro-inflammatory macrophage metabolism, we performed a qPCR analysis of the influence of siHPTs@ZA hydrogel on the expression of M1 phenotype markers (IL-1β, IL-6, and iNOS). In all three cases, siHPTs@ZA hydrogel (group IV) exhibited the highest inhibitory activity (Figure 4F). A similar trend was observed by flow cytometry analysis of M1 surface marker CD86 (Figure 4G), confirming significant suppression of M1 polarization. In line with the examination of the expression of HIF-1α, GLUT1, and PKM2, for IL-1β, IL-6, iNOS, and CD86, we also detected some inhibitory activities for individual components of siHPTs@ZA hydrogel [the highest for siHPTs (group III) and Alg-siHPTs (group II)]. However, the highest efficiency was always reached only when using fully optimized siHPTs@ZA hydrogel, which highlights the importance of the whole assembly. Together the results demonstrate that siHPTs@ZA hydrogel is capable of inhibiting M1 polarization by blocking the glycolytic pathway.

2.6. Promotion of Lipid Metabolism and M2 Polarization

In contrast to the above-explored metabolic properties of M1 macrophages, FAO pathway represents the main metabolic pathway in anti-inflammatory M2 macrophages.[53] Notably, zinc ions are known to act as an essential PPARγ agonist driving transcriptional functions of PPARγ through PPAR's DNA-binding domain ([55]), thus up-regulating the lipid metabolism of M2 macrophages (**Figure** 5A).[55–57] Considering the fact that mitochondria are crucial for FAO pathway, we first determined the content of ATP in IL-4-induced M2 macrophages. As shown in Figure 5B, IL-4-mediated M2 polarization resulted in an increase in ATP content, which was further increased by treatment with siHPTs@ZA hydrogel. Then, we explored the fatty acid accumulation in intracellular lipid bodies, whose processing is a signal of ongoing FAO metabolism. For this purpose, lipid bodies were stained using BODIPY 493/503 and as shown in Figure 5C, siHPTs@ZA hydrogel exposure resulted in highly efficient stimulation of FAO resulting in the disappearance of lipid bodies in M2 macrophages. As stated above, zinc ions stimulate PPARγ expression. Thus, we hypothesized that due to a sustained release of zinc, siHPTs@ZA hydrogel could be able to promote PPARγ expression. Indeed, it was found that PPARγ expression increases in M2 macrophages treated with siHPTs@ZA hydrogel (group IV) (Figure 5D; **Figures** S14 and S15, Supporting Information), indicating that the hydrogel efficiently affects the storage and processing of fatty acids. Subsequently, we sought to confirm the M2 polarization of macrophages exposed to siHPTs@ZA hydrogel. Figure 5E demonstrated the qPCR data showing the expression of mRNA encoding M2 polarization markers ARG-1, CD206, and IL-10. Indeed, it was found that compared to untreated control, siHPTs@ZA hydrogel stimulates the expression of M2 polarization markers. Increased surface expression of CD206 was subsequently confirmed at the protein level using flow cytometry (Figure 5F). Overall, in vitro experiments provided a solid basis indicating that siHPTs@ZA hydrogel efficiently inhibits glycolysis and M1 polarization while stimulating FAO and M2 polarization of anti-inflammatory macrophages.

2.7. Evaluation of In Vivo Biodistribution of siHPTs@ZA Hydrogel

To assess the long-term performance of the siHPTs@ZA hydrogel in vivo, we conducted biodistribution and targeting experiments, both in healthy and collagen-induced arthritis (CIA) rats. We hypothesized that the acidic microenvironment developed at the ankle joints of CIA rats could effectively trigger the biodegradation of siHPTs@ZA hydrogel promoting the release of zinc ions and TNF-α siRNA. As shown in **Figure** 6A, after the intra-articular injection, in both groups, the FITC-labeled siHPTs@ZA hydrogel exhibited strong in situ fluorescence 12 h postadministration. Due to ongoing biodegradation and elimination, the fluorescence signal gradually weakened and nearly disappeared at day 8. ex vivo imaging further confirmed no bioaccumulation in extracted organs, confirming no observable, unwanted diffusion from the administration site, and slightly higher fluorescence signal in joints of CIA rat, which could be plausibly explained by altered metabolism due to ongoing inflammation.

2.8. In Vivo Therapeutic Efficacy of siHPTs@ZA Hydrogel

For consequent assessment of the in vivo therapeutic efficacy of the siHPTs@ZA hydrogel, we again employed CIA rat. It is worth noting that CIA rats displayed classical RA symptoms such as cartilage degradation, bone erosion, and synovial fibrosis. For experiments, the CIA rat was randomly divided into 5 groups, which were separately treated with PBS (G2), ZA (G3), Alg-siHPTs hydrogel (G4), siHPTs (G5) or siHPTs@ZA hydrogel (G6) all via intra-articular injection (schematically depicted in Figure 6B). In all experiments, G1 describes healthy non-arthritic rats. Figure 6C summarized the comparative evaluation of the progression of inflammation in CIA rats versus the state of healthy rats between day 25 (first intra-articular administration) to day 37 (termination). Digital photographs clearly show visible swelling of the hind paws of CIA rats at day 25, which was not observable for healthy rats. The photographs demonstrate that after the last administration of siHPTs@ZA hydrogel (G6), the hind paws' visual appearance did not indicate any signs of inflammation and resembled the hind paws of the healthy rat. One of the features of ongoing inflammation is the temperature increase. Thus, we monitored the temperature of hind paws using a near-infrared imaging system, which confirmed that at the experimental end-point, the local temperature of siHPTs@ZA hydrogel-administered rate decreased to approx. 33 °C, which is comparable to the local hind paw temperature of a healthy rat, indicating the elimination of synovial inflammation. Importantly,

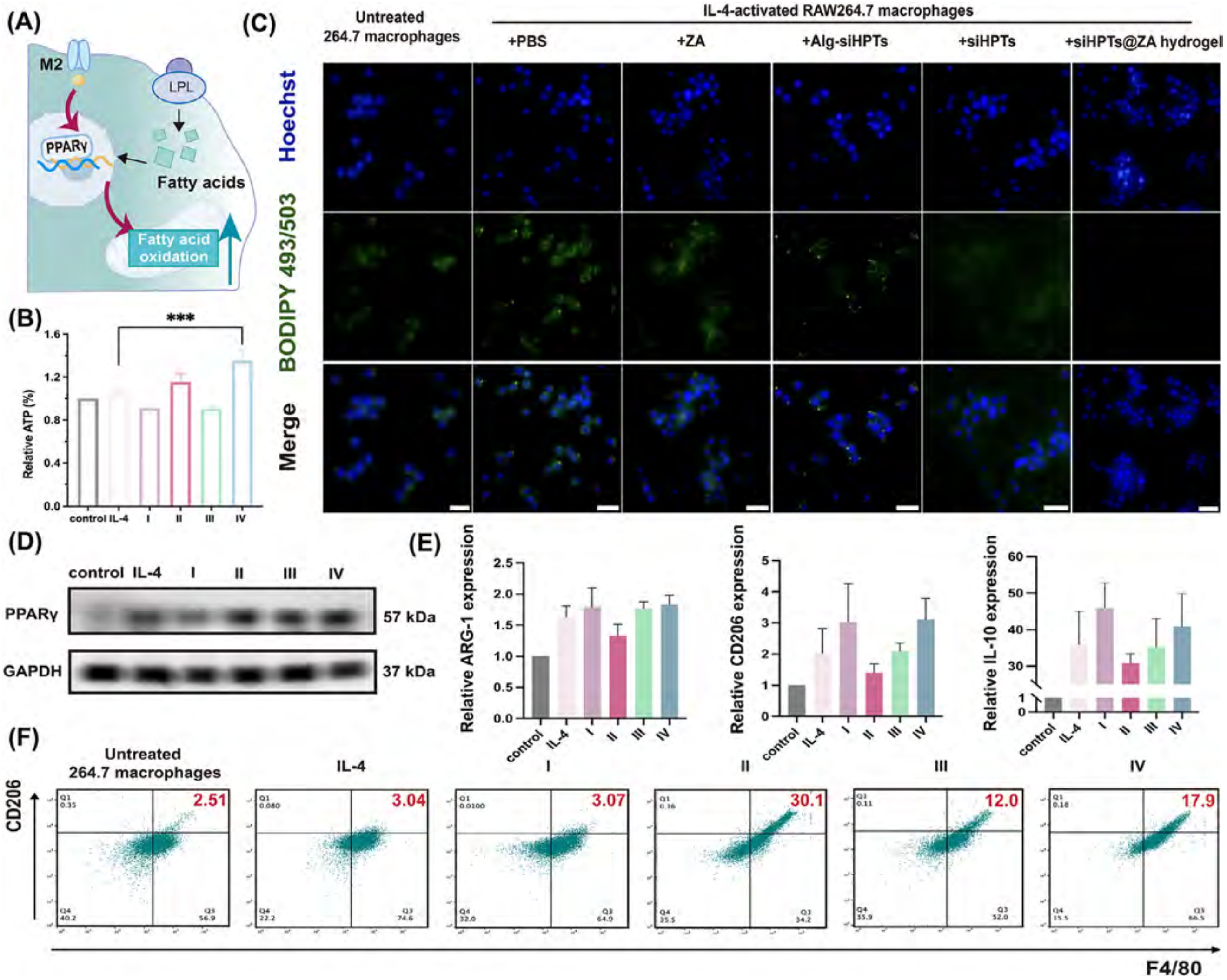

Figure 5. Promotion of lipid metabolism and M2 polarization in RAW264.7 macrophages. A) Schematic depiction of the FAO pathway in M2 macrophages. B) ATP production in RAW264.7 macrophages. The data are expressed as mean ± SD ($n = 3$) represented by error bars. C) Representative micrographs of intracellular lipid droplets stained with BODIPY 493/503 in RAW264.7 macrophages (scale bar, 20 µm). D) Western blot of PPARγ in RAW264.7 macrophages. GAPDH, loading control. E) Relative expression of M2 macrophage markers detected in RAW264.7 macrophages. The data are expressed as mean ± SD ($n = 3$) represented by error bars. F) Flow cytometry dot plots of CD206 expression in RAW264.7 macrophages. Groups: I: ZA, II: Alg-siHPTs, III: siHPTs, IV: siHPTs@ZA hydrogel.

siHPTs@ZA hydrogel not only decelerated RA progression but caused complete remission, which was not observable for the rest of the treatment groups. These retained some extent of hind paws swelling and redness. This might be attributed to the rapid elimination of G3-G5 treatments from the joints through systemic diffusion, confirming the superb properties of siHPTs@ZA hydrogel. The average arthritis clinical scoring of individual groups is shown in the heat map in Figure 6D. In addition, we also recorded hind paw thickness and body weight (Figure 6E,F). It was found that at the experimental end-point, the paw thickness (15.466 mm) of siHPTs@ZA hydrogel-administered rat decreased to 8.53 mm, which was the closest to the healthy rat. Moreover, during the treatment with siHPTs@ZA hydrogel, the body weight of the rat gradually increased, whereas the body weight of the CIA rat decreased due to the ongoing inflammation.

To further understand the therapeutic process, we evaluated the bone erosion and calculated bone mineral density (BMD) of hind paws using micro-computed tomography (micro-CT) **Figure** 7A. The 3D reconstructed micro-CT images revealed a rough surface of obvious ankle erosion and bone loss in G2-G5 groups. In contrast, siHPTs@ZA hydrogel-treated group presented a smoother joint surface, revealing that bone erosion was significantly relieved. Further, the joints were examined using histopathological analysis to evaluate typical RA-associated pathological features, including, extensive pannus formation and severe bone destruction. As shown in Figure 7B hematoxylin and eosin (H&E) staining of joints of CIA rat, confirmed severe tissue deterioration not observable in siHPTs@ZA hydrogel group. To examine the cartilage fitness, we further stained the tissues with Safranin-O (Figure 7C), which revealed extensive cartilage destruction, presented as a rough and irregular pattern in PBS,

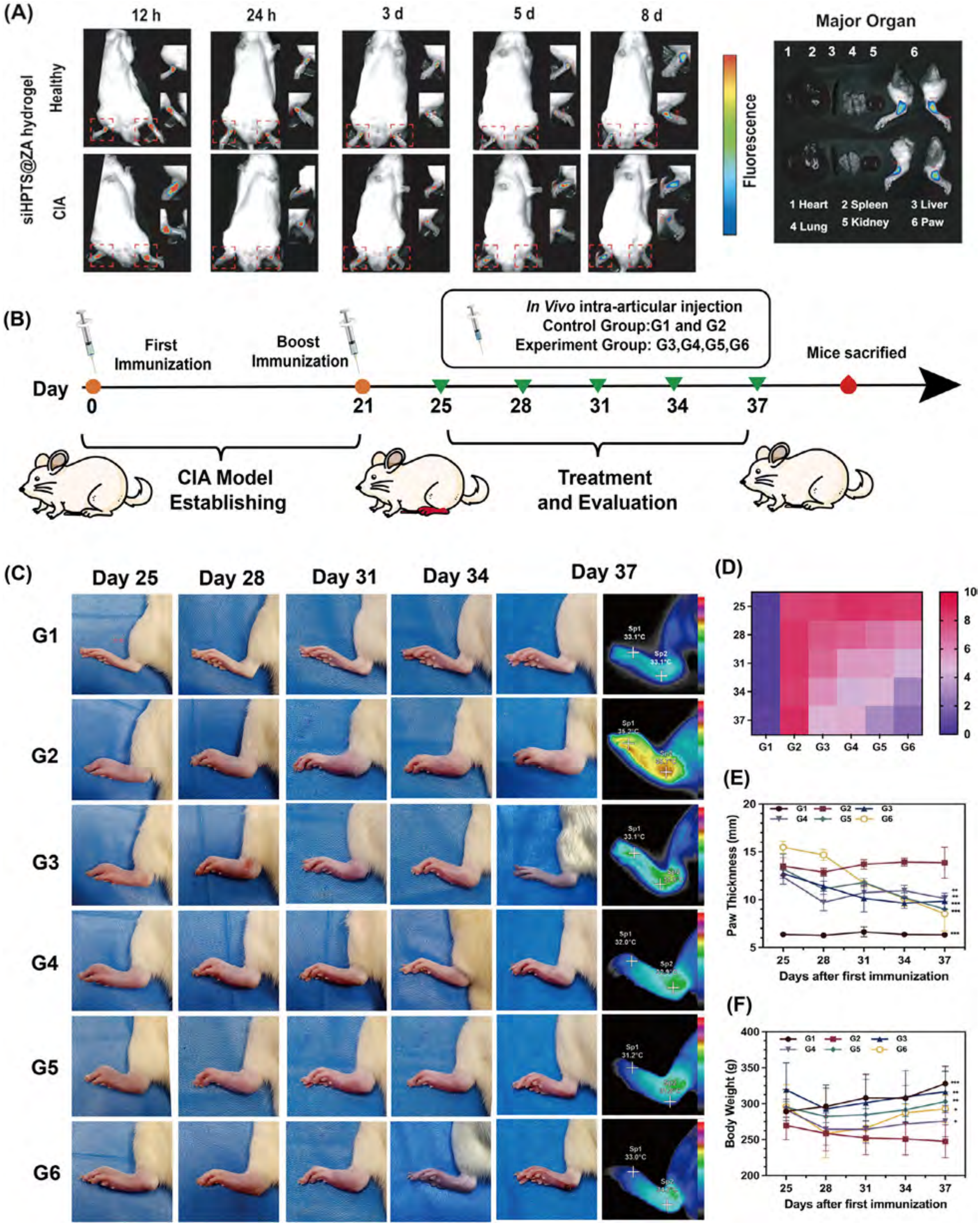

Figure 6. A) In vivo fluorescence imaging showing the presence and ongoing biodegradation and elimination of FITC-labeled siHPTS@ZA hydrogel present in both CIA rats and healthy rats. The right part of the figure shows ex vivo imaging of extracted organs and paws. B) Experimental pipeline of evaluation of therapeutic efficacy. C) Representative digital photographs and thermal images of healthy and CIA rats' hind paws during the treatment course. D) Average arthritis clinical score of individual groups. E) The paw thickness evaluation and F) the variation of body weights. Groups: G1: Healthy control, G2: RA model, G3: ZA hydrogel, G4: Alg-siHPTs, G5: siHPTs and G6: siHPTs@ZA hydrogel. The data are expressed as mean ± SD ($n = 3$) represented by error bars, $^{*}p < 0.05$, $^{**}p < 0.01$, $^{***}p < 0.001$.

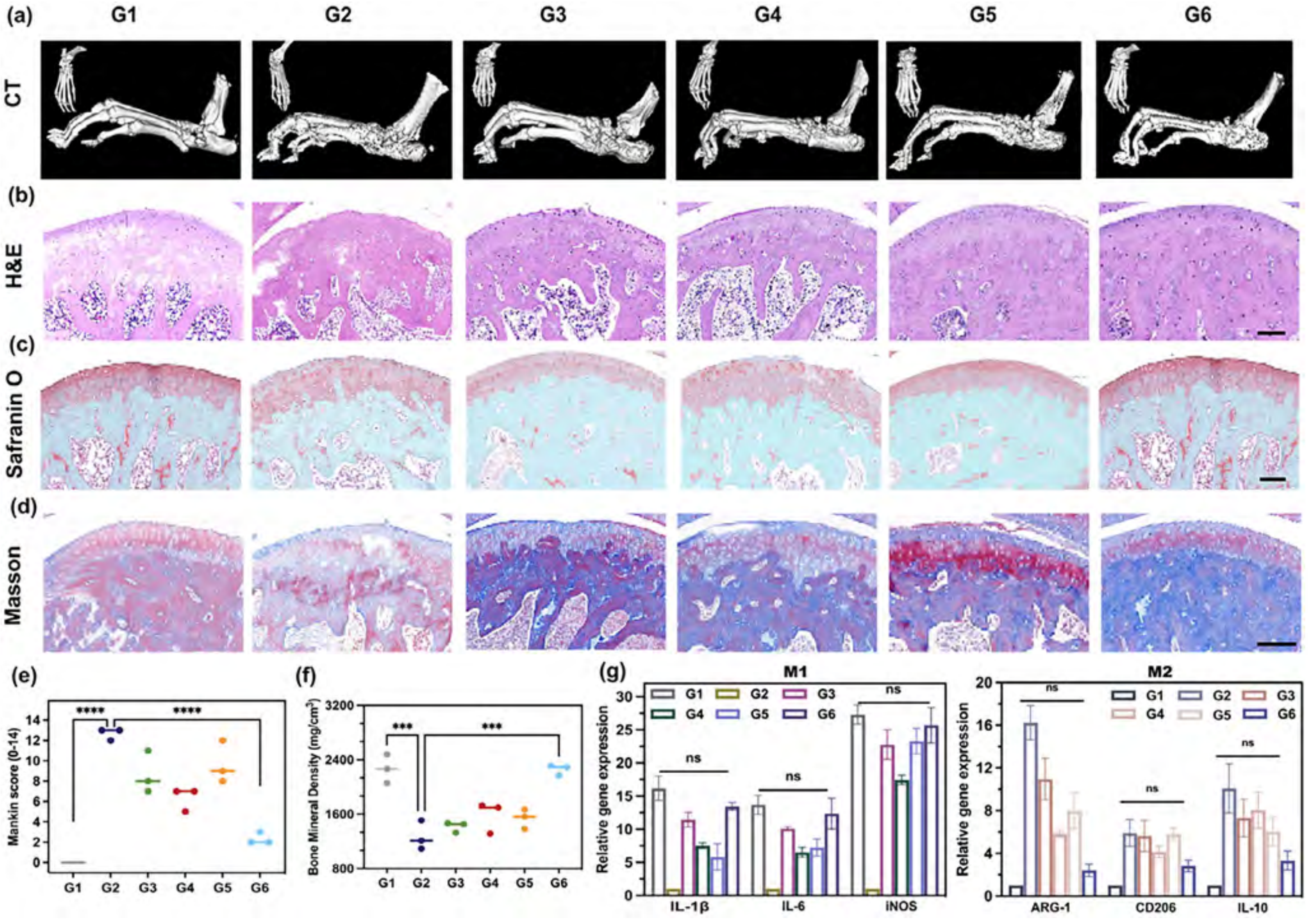

Figure 7. A) Micro CT imaging of bone erosion of hind paws of rats analyzed at the experimental end-point. Histopathological analysis of extracted joints stained with B) H&E, C) Safranin-O, and D) Masson´s trichrome. Scale bars: 100 µm. E) MANKIN scores of individual groups. F) BMD values of the hind paws. G) Relative expression of M1 (IL-1β, IL-6 and iNOS) and M2 (ARG-1, CD206 and IL-10) polarization markers in murine serum. Groups: G1: Healthy control, G2: RA model, G3: ZA hydrogel, G4: Alg-siHPTs, G5: siHPTs and G6: siHPTs@ZA hydrogel. The data are expressed as mean ± SD ($n = 3$) represented by error bars, $***p < 0.001$, $****p < 0.0001$; ns = no significance).

ZA, Alg-siHPTs and siHPTs treated CIA rats. In contrast, the rats treated with siHPTs@ZA hydrogel displayed smooth cartilages with only negligible proteoglycan loss. In addition, Masson´s trichrome staining of the CIA rats treated with siHPTs@ZA hydrogel showed a remarkable recovery of synovial hyperplasia with a clear interface (Figure 7D). The overall MANKIN scoring assessing cartilage structure, cellularity, Safranin-O, and tidemark integrity,[58] was further evaluated and is presented in Figure 7F. It clearly demonstrates that siHPTs@ZA hydrogel-based therapy was able to reach MANKIN score of 2.3, which is close to the normal physiological status (0.0). MANKIN scoring also demonstrated that while the performance of the rest of the treatment groups (G3-G5) might look efficient, a complex evaluation of joint status is needed to fully appreciate the efficacy of siHPTs@ZA hydrogel. This statement was further corroborated by BMD analysis confirming a decrease in bone erosion due to siHPTs@ZA hydrogel administration (Figure 7E).

In addition, we also assessed the efficiency of metabolic reprogramming in extracted joint tissues. As shown in Figure S16 (Supporting Information), siHPTs@ZA hydrogel-treated rats exhibited the lowest expression of GLUT1 and the highest expression of PPARγ confirming the ability of hydrogel to induce metabolic reprogramming in vivo. Further, to determine the effect of siHPTs@ZA hydrogel administration on macrophage polarization, levels of serum cytokines were analyzed. As shown in Figure 7G, the amounts of M1 polarization markers (IL-1β, IL-6, and iNOS) were dramatically reduced after siHPTs@ZA hydrogel treatment to the amounts close to the healthy animals, confirming strong suppression of M1 polarization. On the other hand, the amount of M2 polarization markers (CD206, ARG-1, and IL-10) was markedly upregulated, highlighting the superior ability of siHPTs@ZA hydrogel to induce M2 polarization, which was also observable at the in vitro level. Importantly, we also corroborated the in vitro results and found out that the siHPTs@ZA hydrogel successfully downregulated TNF-α in rat joints (Figure S10, Supporting Information).

2.9. Biosafety Evaluation siHPTs@ZA Hydrogel

Although we did not expect side effects due to stable bioaccumulation of siHPTs@ZA hydrogel in joints, which was observed in previous experiments, we finally evaluated possible side effects that could be caused by biodegradation into smaller non-detected molecules diffusing to the blood circulation. For this purpose, at the experimental end-point, we collected the selected organs (heart, liver, spleen, lung, and kidneys) and performed histopathological examination after H&E staining. As displayed in Figure S18 (Supporting Information), for all treatment groups, organ sections showed no histopathological abnormalities, which corroborated the biosafety of siHPTs@ZA hydrogel even after repeated intra-articular injection.

3. Conclusion

In summary, the study demonstrates the preparation and comprehensive testing of siHPTs@ZA hydrogel for intra-articular injection for RA therapy. We show that hydrogel is capable of reprogramming RA microenvironmental immunometabolism toward decreased hypoxia, glycolysis, and enhanced FAO pathway and M2 macrophage polarization. Complex preclinical evaluation in RA rats confirmed that siHPTs@ZA hydrogel acts as a highly potent therapeutic modality reversing the pathological features of RA. Considering the biophysical properties of the assembled hydrogel, it can be expected that it could be used for loading with other RNA interference effectors and plausibly with other low-mass bioactive molecules to further improve the biological properties of hydrogel toward next-generation therapy of RA.

4. Experimental Section

Materials: PEGDA (Mw = 700) (PEGDA700, 98%) was obtained from Meryer (China). Liquid paraffin, Span-80, and Tween-80 were provided from HEOWNS (China). Cystamine and dimethyl sulfoxide (DMSO) were bought from Sigma-Aldrich (China). Methanol and ethanol (99.5%) were obtained from Tianjin Yuanli Chemical Co., Ltd. (China). Dichloromethane (CH_2Cl_2) was purchased from Macklin Biochemical Technology Co., Ltd. (China). Fetal bovine serum (FBS) and penicillin/streptomycin were obtained from Procell (China). Primers used for qPCR, TNF-α siRNA, Lipo2000, and FAM-labeled siRNA were purchased from Sangon Biotech Co., Ltd. (China). ABScript Neo RT Master Mix and 2XUniversal SYBR Green Fast qPCR Mix were bought from ABclonal (China). Zinc Colorimetric Assay Kit, FITC anti-mouse CD86 antibody, and FITC anti-mouse CD206 antibody were obtained from Elabscience (China). HIF-1α mouse monoclonal antibody was acquired from Beyotime (China). CCK-8 assay kit, Hoechst 33342, and LysoTracker Red were provided by Solarbio Life Science and Technology Ltd. (China). BODIPY 493/503 was obtained from GlpBio (USA). All materials were used without further purification.

Formulation of siHPTs@ZA Hydrogel—Synthesis of siHPTs: According to a previous study, the HB-PBAE was synthesized by the A2+B4 Michael addition with the molar ratio of diacrylate to amine groups of 2.5:1. The PEGDA (1.976 g) and cystamine (967.4 mg) were added to the brown vial and dissolved in 6 mL of DMSO (6 mL). The reaction was carried out for 24 h in the dark at 95 °C under continuous stirring. Then, the reaction mixture was slowly added to ether and shaken vigorously, centrifuged (3500 rpm, 5 min) and the precipitate was collected. This process was repeated five times to remove residual DMSO and unreacted monomers. The product was dried under a vacuum. After HB-PBAE synthesis, it was loaded with TNF-α siRNA through electrostatic adsorption. Briefly, TNF-α siRNA and HB-PBAE were dissolved in DEPC-treated water at the concentration of 0.1 and 1 mg mL^{-1}, respectively. The solution was mixed while vortex stirring for 90 s. After 1 h of incubation at room temperature, the siHPTs were acquired.

Formulation of siHPTs@ZA Hydrogel—Synthesis of siHPTs@ZA Nanospheres: Firstly, the aqueous phase was prepared by weighing 1.00 g sodium alginate adding it to 100 mL double-distilled water, and kept in a water bath at 45 °C for 6 h. After that, it was restored to room temperature and placed into the refrigerator, where it was kept at 4 °C overnight to allow for full solubilization. Then, the oil phase was formed by adding 50 mL liquid paraffin, 0.28 mL Span-80, and 0.15 mL Tween-80 to a 250 mL three-necked flask in a water bath at 40 °C, while stirring (500 rpm, 30 min). Then the oil phase was completely mixed with the water phase. For this, the oil phase was stirred at 1000 rpm at 40 °C, and using the flow rate of 0.75 mL min^{-1} in a microfluidic chip through the peristaltic pump, it was employed to slowly drip the water phase into the oil phase. Then, stirring continued for 1 h to allow for full mixing of two phases. Next, the cross-linking agent was prepared by weighing 0.025 g of anhydrous zinc chloride and mixing it with siHPTs in 10 mL of 95% ethanol. 5 mL of the cross-linking agent was then added drop by drop into the above mixture by the microfluidics (flow rate of 0.25 mL min^{-1}), and stirred for 1 h. The final emulsion was centrifuged (3800 rpm, 10 min), and the lower layer of liquid containing siHPTs@ZA nanospheres was collected and freeze-dried in a lyophilizer and stored at 4 °C prior to further use.

Formulation of siHPTs@ZA Hydrogel—Synthesis of siHPTs@ZA Hydrogel: Dried siHPTs nanospheres were weighed and placed in a mold, to which 8% wt of siHPTs@ZA nanospheres solution was added dropwise until the system fully absorbed water and reached an equilibrium state of solubility. The resulting assembly was the injectable siHPTs@ZA hydrogel.

Physico-Chemical Characterization of siHPTs@ZA Nanospheres and HB-PBAE: The morphology and size of the siHPTs@ZA nanospheres were examined using TEM (JEM100CXII, Jeol Ltd., Japan) and Zetasizer Nano-ZS (Malvern Instruments, UK), which was also employed for zeta potential analyses. HB-PBAE was characterized by ^{1}H-NMR (Bruker Advance 400 MHz, Germany) and using GPC (Waters, USA). In addition, the elemental composition of siHPTs@ZA nanospheres was analyzed using EDS (Tecnai G2 F20 U-Twin, FEI, USA). The absorption spectra were recorded using UV-Vis spectrophotometer (Agilent, USA). FT-IR (TENSOR 27, Bruker, Germany), Raman (Renishow, inVia reflex, UK), and CD spectra (Biotools, Seyssinet-Pariset, France) were recorded too to describe physicochemical properties of siHPTs@ZA nanospheres.

Agarose Gel Electrophoresis: The loading of siRNA to HB-PBAE was investigated by agarose gel electrophoresis. For this, 5× loading buffer was added to 10 µL of analyzed samples. The samples were then loaded onto a 0.8% agarose gel and separation was carried out in 1× TAE running buffer at 120 V for 30 min. The gels were visualized under UV light at 254 nm using an Image master VDS thermal imaging system (Bio-Rad, USA).

Physico-Chemical Characterization of siHPTs@ZA Hydrogel: SEM micrographs were obtained using a SU8020 SEM (Hitachi, Japan). The storage modulus, loss modulus, and viscosity of hydrogels were detected by an advanced rotational rheometer (Anton Paar, MCR302, Austria). To test degradation, siHPTs@ZA nanospheres were prepared with different concentrations of ZA. 1.8 g of each formulation of dry hydrogel was then added to 18 mL of PBS and placed on a constant temperature shaker. Then, 3 mL of samples were collected at a fixed point (1, 2, 3, 4, 5, and 8 days) and weighted after vacuum drying to count the degradation rate. To determine the equilibrium swelling ability, the lyophilized siHPTs@ZA hydrogels were weighted (m1) and volume was recorded (v1). Then, hydrogels were placed into the dish and incubated in PBS at 37 °C. At reached equilibrium, the solution was removed from the dish. Next, hydrogels were weighted again (m2) and the volume (v2) was recorded. The mass swelling ratio was then calculated as (m2-m1)/m1 × 100%, while the formula used to calculate volume swelling was (v2-v1)/v1 × 100%. The release of zinc ions from siHPTs@ZA hydrogel was in determined in the supernatant using a Zinc Colorimetric Assay kit (E-BC-K-137-M, Elabscience) according to the manufacturer's instruction.

Cell Culture Conditions and Macrophages Polarization: Murine macrophages (RAW264.7) were obtained from Solarbio Technology Co., Ltd. (China). The cells were cultured in fresh Dulbecco's Modified Eagle Medium (DMEM) supplemented with 10% FBS and 1% penicillin/streptomycin at 37.1 °C in a 5% CO_2. To induce polarization, the M1 macrophages were established by treating RAW264.7 cells with 2.5 ng mL^{-1} of IFNγ and 200 ng mL^{-1} LPS (Sigma, USA). M2 macrophages were obtained by induction using 20 ng mL^{-1} IL-4 (Thermo Fisher Scientific, USA).

Uptake, Intracellular Fate, and Cytotoxicity Assessment: To evaluate the siHPTs@ZA hydrogels' cellular uptake, RAW264.7 macrophages were cultivated on CLSM culture dishes. After reaching a density of ≈1 × 10^5 cells per well, the culture medium was exchanged with a serum-free medium containing FITC-labeled siHPTs@ZA nanospheres, and the cells were incubated for another 12 h. At 0, 2, 4, 8, and 12 h time points, cells were fixed, and washed with PBS, and nuclei and endolysosomes were stained using Hoechst 33342 and Lysotracker Red, respectively. Then, the cells were washed and stained with PBS three times and observed under CLSM (Leica SP 8, Leica, Germany).

To investigate the cytotoxicity of siHPTs@ZA hydrogel, a CCK-8 assay was conducted. First, the cells were seeded into 96-well plates at a density of 1 × 10^4 cells per well. Then, annotated treatments were added to each well. After incubation 6, 12, and 24 h), CCK-8 reagent (20 µL) was added into each well and the cells were cultured for another 4 h.

Evaluation of Transfection and Knock-Down Efficiency: To verify the siRNA transfection, FAM-labeled siRNA was used to formulate siHPTs@ZA hydrogels using various w/w ratios of ZA and siHPTs (1:1, 1:2, 1:4, and 1:8). In all experiments, Lipo2000 and naked FAM-labeled siRNA were used as positive and negative control, respectively. Next, RAW264.7 macrophages were seeded into the CLSM dishes (1 × 10^5 cells per well), followed by incubation in DMEM supplemented with 10% FBS. To evaluate the transfection, DMEM was exchanged with annotated treatments in Opti-MEM. After 6 h incubation, the medium was discarded, and the cells were washed with PBS three times. Then, nuclei were counterstained with Hoechst 33342 and the cells were observed under CLSM. After that, CCK-8 assay was carried out as already described above to assess the cytotoxicity of siHPTs@ZA hydrogels differing in ZA-to-siHPTs ratio for RAW264.7 macrophages. Finally, knock-down efficiency was analyzed by evaluating the expression of TNF-α at the mRNA and protein levels as described below.

Evaluation of Glucose, Pyruvate, and ATP In Vitro: To evaluate the number of energetic metabolites, polarized M1 and M2 RAW264.7 macrophages were seeded in a 6-well plate at a density of ≈1 × 10^5 cells per well and cultured with annotated treatments for 12 h. Then, the cells were washed using PBS and harvested for analysis of glucose and pyruvate (for M1 macrophages) using a D-Glucose Content Assay Kit (AKSU001C, Boxbio) and a Pyruvate Content Assay Kit (BC2200, Solarbio) according to the manufacturer's instructions. In M2 macrophages, ATP was quantified using an ATP Detection kit (S0026, Beyotime) according to the manufacturer's instructions.

Immunofluorescence and Lipid Droplet Staining: RAW264.7 macrophages were seeded onto confocal dishes at a density of 1 × 10^4 cells per well and polarized into M1 or M2 phenotype as described above. Then, the cells were treated with annotated treatment groups (normalized to 200 µg mL^{-1}). After 12 h incubation, the cells were washed with PBS and fixed with 4% paraformaldehyde, permeabilized with 0.1% Triton X-100 for 15 min, and blocked using 4% bovine serum albumin for 30 min at room temperature. Between each step, cells were rinsed with PBS three times. Subsequently, cells were immunolabeled using the primary rabbit anti-GLUT1 antibody (100×, SA0377, Huabio) and mouse anti-HIF-1α antibody (100×, AG2135, Beyotime) at 4 °C overnight. Then, the cells were washed with PBS and incubated with horseradish peroxidase-conjugated secondary goat anti-rabbit IgG H&L (1000×, iFluorTM 488, HA1121, Huabio) or anti-mouse IgG H&L (1000×, A0216, Beyotime) for 1 h. Hoechst 33342 was used for nuclei counterstain and the cells were observed under CLSM. To determine the amount of intracellular lipid bodies, RAW264.7 macrophages were seeded in confocal cell dishes at a density of 1 × 10^4, and polarized to M2 phenotype as described above. After reaching ≈60%-75% confluence, the medium was removed, and the cells were washed with PBS twice. Then, 1 mL of BODIPY 593/503 working solution was added and the cells were incubated at room temperature for 30 min. Nuclei were counterstained using Hoechst 33342 and the cells were observed under CLSM.

Western Blotting: For Western blotting, proteins were isolated after lysis using lysis buffer (RIPA: PMSF = 1000:1) and the concentration of proteins was quantified using a BCA Protein Assay Kit. Before immunoblotting, proteins were separated using sodium dodecyl sulfate-polyacrylamide gel electrophoresis and then transferred to poly(vinylidene fluoride) (PVDF) membranes. Next, membranes were blocked using BSA and incubated with specific primary antibodies: TNF alpha (1000×, ER1919-22, HUABIO), GLUT1, HIF-1α, PKM2 (1000×, 1F2-F4-H11, OriGene), PPARγ (5ab209350, Abcam) and GAPDH (1000×, AF3006, Beyotime) at 4 °C overnight. Then, the membranes were washed and incubated with appropriate horseradish peroxidase secondary antibodies for 3 h at room temperature. The protein signal was developed using ECL plus kit (Amersham, USA) and visualized using the Bio-Rad ChemiDoc MP System (Bio-Rad, USA).

Macrophage polarization markers detection—Flow Cytometry: RAW264.7 macrophages were seeded (1 × 10^6 cells per well) in 6-well plates and cultured overnight. Each group of M1 or M2 macrophages polarized as described above was treated with annotated treatments (normalized to 200 µg mL^{-1}, 12 h). Afterward, the cells were immunostained with APC-labeled F4/80 antibodies (20x) and FITC-labeled anti-human CD86 antibodies (20x) or FITC-labeled anti-human CD206 antibodies (20x) at room temperature for 30 min without permeabilization. Then, the cells were collected by centrifugation and washed with PBS. Expression of polarization markers was carried out using flow cytometry (BD FACSAria III, USA).

Macrophage polarization markers detection—qPCR: To evaluate the expression of mRNA encoding analyzed polarization markers, macrophages polarized and treated as described above, mRNA was extracted using TRIzol, and cDNA was synthesized using ABScript III ReverseTranscriptase B (ABclonal RK26501) according to the manufacturer's instructions. Then, Ultra SYBR Green and primers were added qPCR was run using qPCR cycler (Applied Biosystems) according to the following conditions: predenaturing at 95 °C for 3 min, denaturing at 95 °C for 5 s, 45 cycles, annealing at 60 °C for 30 s, 45 cycles.

Evaluation of siHPTs@ZA Hydrogel Hemolytic Properties: Blood was collected from healthy rats and centrifuged at 2000 rpm for 10 min four times to separate erythrocytes. Subsequently, after several washing steps with 0.9% saline, the erythrocytes were diluted to 10% with PBS. Next, 200 µL of erythrocyte suspension was mixed with 800 µL of PBS (negative control), deionized water (positive control), and annotated concentrations of siHPTs@ZA hydrogel. Then, erythrocytes were incubated for 2 h at 37 °C. After that, samples were centrifuged at 12000 rpm for 10 min, followed by supernatant collection and analysis of its absorption at 570 nm. The percentage of hemolysis was calculated according to the following formula: $(A_{\text{sample}} - A_0)/\ (A_{100} - A_0) \times 100\%$.

CIA Preclinical Rat Model of RA: Male Sprague-Dawley rats (6–8 weeks old) were sourced from Huafukang Biological Technology Co., Ltd. (Beijing, China) and kept at the Laboratory Animal Center of the Chinese Academy of Medical Sciences Institute of Radiology in Tianjin. All animal experiments adhered to the guidelines for the Care and Use of Laboratory Animals at the institute. The protocols were reviewed and approved by the animal ethics committee of Tianjin University (approval no. (SYXK-2019-0002)).

For the first immunization, bovine type II collagen solution (CII; Chondrex, Inc.) mixed with complete Freund's adjuvant (HY-153808, MedChemExpress) in 1:1 ratio, was administered subcutaneously via the tail root. 21 days later, booster immunization was done by injection of incomplete Freund's adjuvant (HY-153808A, MedChemExpress) mixed with bovine type II collagen into the tail vein resulting in to establishment of the CIA model characterized by progressive RA.

In Vivo and Ex Vivo Fluorescence Imaging: To detect the biodistribution after intra-articular administration, FITC-labeled siHPTs@ZA hydrogels (100 µL, 1 mg mL^{-1}) were injected into the joints of healthy and CIA rats. Then, time-dependent fluorescence images of hind paws were captured at various time points (12 h, 24 h, 3 days, 5 days, and 8 days) using the IVIS Lumina imaging system (Caliper, USA). After 8 days, rats were sacrificed and selected organs including heart, liver, spleen, lung, and kidney were excised and ex vivo imaged to determine possible unwanted diffusion from joints to blood circulation and organs.

In Vivo Therapeutic Efficacy: To evaluate the therapeutic efficacy of siHPTs@ZA hydrogels, rats were randomly divided rat into six groups (G1: Healthy rat treated with PBS, G2: CIA rat treated with PBS, G3: CIA rat treated with ZA, G4: CIA rat treated with Alg-siHPTs, G5: CIA rats treated with siHPTs and G6: CIA rats treated with siHPTs@ZA hydrogel) and orthotopically injected into the joint cavity with a formula dose of 10 mg kg^{-1}. During the treatment period, each rat was weighted, and paw thickness and clinical arthritic scores were recorded. The arthritis scoring was assessed based on the following scale: 0 = normal, 1 = mild redness and swelling confined to the ankle joint, 2 = slight redness and moderate swelling extending from the ankle to the tarsal region, 3 = erythema and noticeable swelling spreading from the ankle to the metatarsal joints, and 4 = prominent redness and swelling affecting the ankle, foot, and toes, or ankylosis of the limb, indicating the highest level of inflammation.[59] Simultaneously, the temperature of the hind paws was analyzed using an infrared thermal camera. Moreover, after the experiment termination, micro-CT images were acquired by a micro-CT scanner (Quantum FX, PerkinElmer, USA).

Finally, at the experimental endpoint, all rats were euthanized and their ankle joints and major organs were collected for subsequent analyses. The ankle joints were decalcified using a 10% EDTA solution, embedded in paraffin, and then sectioned. Subsequently, these sections were stained using H&E, Safranin O-fast green assay or Masson's trichrome staining. In addition, serum from the rat was obtained after centrifugation and performed qPCR evaluation gene expression level of the M1 (IL-6, IL-1β, and iNOS) and M2 (ARG-1, IL-10, and CD206) phenotype markers as described above.

Statistical Analysis: Results are expressed as the mean ± standard deviation (SD). To evaluate the results, an analysis of variance was utilized. 2-Sample t-test was utilized to calculate the p values. The significant difference was represented by the probability level of 95%.

Supporting Information

Supporting Information is available from the Wiley Online Library or from the author.

Acknowledgements

This work was supported by the National Natural Science of China (No. 82273873), Tianjin Youth Science and Technology Talents (QN.20230215), and the Czech Science Foundation (project. no. 23-04740M).

Open access publishing facilitated by Mendelova univerzita v Brne, as part of the Wiley - CzechELib agreement.

Conflict of Interest

The authors declare no conflict of interest.

Data availability statement

The data that support the findings of this study are available from the corresponding author upon reasonable request.

Keywords

fatty acid oxidation, glycolysis, hydrogels, metabolic reprogramming, rheumatoid arthritis

Received: January 30, 2025
Revised: February 27, 2025
Published online: March 10, 2025

[1] K. O'Leary, *Nat. Med.* **2023**.
[2] A. Sammut, S. Shea, R. S. Blumenthal, M. Szklo, J. M. Bathon, J. F. Polak, R. Tracy, J. T. Giles, *Arthritis Care Res.* **2017**, *69*, 1799.
[3] G. Jones, P. Nash, S. Hall, *Med. J. Australia* **2017**, *206*, 221.
[4] M. Zhang, R. Zhang, Y. Dong, J. Liu, Z. Gao, X. Zhou, J. Cao, *Chem. Eng. J.* **2023**, *459*, 141484.
[5] C.-F. Cheng, H.-J. Liao, C.-S. Wu, *J. Formosan Med. Assoc.* **2022**, *121*, 1027.
[6] J. Tian, T. Chen, B. Huang, Y. Liu, C. Wang, Z. Cui, H. Xu, Q. Li, W. Zhang, Q. Liang, *Acta Biomater.* **2023**, *157*, 367.
[7] K. Wang, C. Yin, X. Ye, Q. Chen, J. Wu, Y. Chen, Y. Li, J. Wang, C. Duan, A. Lu, D. Guan, *Small* **2023**, *19*, 2207319.
[8] Y.-P. Zhao, J.-F. Han, F.-Y. Zhang, T.-T. Liao, R. Na, X.-F. Yuan, G.-B. He, W. Ye, *Drug Deliv.* **2022**, *29*, 2269.
[9] D. Vats, L. Mukundan, J. I. Odegaard, L. Zhang, K. L. Smith, C. R. Morel, D. R. Greaves, P. J. Murray, A. Chawla, *Cell Metab.* **2006**, *4*, 13.
[10] S. A. Clayton, L. MacDonald, M. Kurowska-Stolarska, A. R. Clark, *Front. Media S.A* **2021**, *12*, 673916.
[11] S. Umar, K. Palasiewicz, M. V. Volin, B. Romay, R. Rahat, C. Tetali, S. Arami, M. Guma, C. Ascoli, N. Sweiss, R. K. Zomorrodi, L. A. J. O'Neill, S. Shahrara, *Cell. Mol. Life Sci.* **2021**, *78*, 7693.
[12] X. Chang, C. Wei, *Int. J. Rheum. Dis.* **2011**, *14*, 217.
[13] D. Zheng, J. Hu, C. Mai, L. Huang, H. Zhou, L. Yu, Y. Xie, *Acta Pharmacol. Sin.* **2024**, *45*, 2354.
[14] Y. J. Kim, S. Lee, J. Jin, H. Woo, Y. K. Choi, K. G. Park, *Int. J. Mol. Sci.* **2022**, *23*, 1696.
[15] D. Namgaladze, B. Brüne, *Biochim. et Biophys. Acta (BBA) - Mol. Cell Biol. Lipids* **2016**, *1861*, 1796.
[16] M. Biniecka, M. Canavan, T. McGarry, W. Gao, J. McCormick, S. Cregan, L. Gallagher, T. Smith, J. J. Phelan, J. Ryan, J. O'Sullivan, C. T. Ng, D. J. Veale, U. Fearon, *Ann. Rheum. Dis.* **2016**, *75*, 2192.
[17] A. J. Freemerman, L. Zhao, A. K. Pingili, B. Teng, A. J. Cozzo, A. M. Fuller, A. R. Johnson, J. J. Milner, M. F. Lim, J. A. Galanko, M. A. Beck, J. E. Bear, J. D. Rotty, L. Bezavada, H. S. Smallwood, M. A. Puchowicz, J. Liu, J. W. Locasale, D. P. Lee, B. J. Bennett, E. D. Abel, J. C. Rathmell, L. Makowski, *J. Immunol.* **2019**, *202*, 1265.
[18] Z. Chen, J. Dudek, C. Maack, U. Hofmann, *Biochem. Pharmacol.* **2021**, *190*, 114597.
[19] K. Balamurugan, *Int. J. Cancer* **2016**, *138*, 1058.
[20] Z. Wang, M. Wang, X. Xu, Y. Liu, Q. Chen, B. Wu, Y. Zhang, *Biochem. Biophys. Res. Commun.* **2023**, *684*, 149128.
[21] Y. Liu, R. Xu, H. Gu, E. Zhang, J. Qu, W. Cao, X.i Huang, H. Yan, J. He, Z. Cai, *Biomark Res.* **2021**, *9*, 1.
[22] Y. Zhou, R. Xiang, G. Qin, B. Ji, S. Yang, G. Wang, J. Han, *Int. Immunopharmacol.* **2022**, *111*, 109137.
[23] P. Bostrom, B. Magnusson, P.-A. Svensson, O. Wiklund, J. Boren, L. M. S. Carlsson, M. Stahlman, S.-O. Olofsson, L. M. Hulten, *Arterioscler Thromb. Vasc. Biol.* **2006**, *26*, 1871.
[24] Y. Li, Y. Pan, X. Zhao, S. Wu, F. Li, Y. Wang, B. Liu, Y. Zhang, X. Gao, Y. Wang, H. Zhou, *Clin. Nutr.* **2024**, *43*, 332.
[25] G. Chinetti, J.-C. Fruchart, B. Staels, *Curr. Opin. Lipidol.* **2003**, *14*, 459.
[26] M. A. Bouhlel, B. Derudas, E. Rigamonti, R. Dièvart, J. Brozek, S. Haulon, C. Zawadzki, B. Jude, G. Torpier, N. Marx, B. Staels, G. Chinetti-Gbaguidi, *Cell Metab.* **2007**, *6*, 137.
[27] Z. Chen, L. Xing, Q. Fan, A. G. Cheetham, R. Lin, B. Holt, L. Chen, Y. Xiao, H. Cui, *Theranostics* **2017**, *7*, 2003.
[28] T. Kim, J. Suh, W. J. Kim, *Adv. Mater.* **2021**, *33*. https://doi.org/10.1002/adma.202008793.
[29] H. Zhou, C. Liang, Z. Wei, Y. Bai, S. B. Bhaduri, T. J. Webster, L. Bian, L. Yang, *Mater. Today* **2019**, *28*, 81.
[30] R. Singh, K. Jadhav, R. Kamboj, H. Malhotra, E. Ray, A. Jhilta, V. Dhir, R. K. Verma, *Biomater. Adv.* **2024**, *160*, 213853.
[31] H. Liu, Y. Liu, Z. Tian, J. Li, M. Li, Z. Zhao, *ACS Appl. Mater. Interfaces* **2024**, *16*, 37656.

[32] J. Lin, L. Chen, J. Yang, X. Li, J. Wang, Y. Zhu, X. Xu, W. Cui, *Small* **2022**, *18*, https://doi.org/10.1002/smll.202202156.
[33] J. Zhang, C. Hurren, Z. Lu, D. Wang, *Int. J. Biol. Macromol.* **2022**, *222*, 1723.
[34] H. Zhang, J. Cheng, Q. Ao, *Mar. Drugs* **2021**, *19*, 264.
[35] N. Taira, K. Ino, J. Robert, H. Shiku, *Electrochim. Acta* **2018**, *281*, 429.
[36] C. Colin, E. Akpo, A. Perrin, D. Cornu, J. Cambedouzou, *Molecules* **2024**, *29*, 2515.
[37] H. Cheng, H. Wu, T. Guo, H. J. Park, J. Li, *Eur. J. Pharm. Biopharm.* **2022**, *179*, 173.
[38] N. Wei, Z. Lv, X. Meng, Q. Liang, T. Jiang, S. Sun, Y. Li, J. Feng, *Int. J. Biol. Macromol.* **2023**, *252*, 126396.
[39] C. Buerkli, S. H. Lee, E. Moroz, M. C. Stuparu, J.-C. Leroux, A. Khan, *Biomacromolecules* **2014**, *15*, 1707.
[40] M. Shi, J. Zhang, Z. Huang, Y. Chen, S. Pan, H. Hu, M. Qiao, D. Chen, X. Zhao, *J. Mater. Chem. B* **2020**, *8*, 1616.
[41] Y. J. Ooi, C. Huang, K. Lau, S. Y. Chew, J. G. Park, M. B. Chan-Park, *ACS Appl. Mater. Interfaces* **2024**, *16*, 14093.
[42] X. Liu, F. Ding, Y. Guo, K. Jiang, Y. Fu, L. Zhu, M. Li, X. Zhu, C. Zhang, *ACS Appl. Bio Mater.* **2022**, *5*, 1857.
[43] C. Wang, X. Wang, K. Dong, J. Luo, Q. Zhang, Y. Cheng, *Biomaterials* **2016**, *104*, 129.
[44] J. Hu, X. Chen, J. Lin, Z. Xu, M. Luo, G. C.-P. Tsui, Y.u Deng, *J. Micromech. Microeng.* **2024**, *34*, 045011.
[45] P. Haloi, B. S. Lokesh, S. Chawla, V. B. Konkimalla, *Drug Deliv.* **2023**, *30*, https://doi.org/10.1080/10717544.2023.2184307.
[46] H. Iwakawa, Y. Tomari, *Mol. Cell* **2022**, *82*, 30.
[47] A. Bohr, N. Tsapis, C. Foged, I. Andreana, M. Yang, E. Fattal, *Eur. J. Pharm. Biopharm.* **2020**, *156*, 114.
[48] D. J. Gorth, I. M. Shapiro, M. V. Risbud, *Cell Death Dis.* **2018**, *10*, 7.
[49] K. Koedderitzsch, E. Zezina, L. Li, M. Herrmann, N. Biesemann, *Sci. Re* **2021**, *11*, 19385.
[50] V. Z. Wall, S. Barnhart, J. E. Kanter, F. Kramer, M. Shimizu-Albergine, N. Adhikari, T. N. Wight, J. L. Hall, K. E. Bornfeldt, *JCI Insight* **2018**, *3*, https://doi.org/10.1172/jci.insight.96544.
[51] H. Li, Q.-Y. Wu, X.-H. Teng, Z.-P. Li, M.-T. Zhu, C.-J. Gu, B.-J. Chen, Q.-Q. Xie, X.-J. Luo, *Cent. Eur. J. Immunol.* **2023**, *48*, 338.
[52] J. E. Toller-Kawahisa, C. H. Hiroki, C. M. D. S. Silva, D. C. Nascimento, G. A. Públio, T. V. Martins, L. E. A. Damasceno, F. P. Veras, P. R. Viacava, F. Y. Sukesada, E. A. Day, A. Zotta, T. A. J. Ryan, R. Moreira da Silva, T. M. Cunha, N. P. Lopes, F. D. Q. Cunha, L. A. J. O'Neill, J. C. Alves-Filho, *Nat. Commun.* **2023**, *14*, 4280.
[53] J. Van den Bossche, L. A. O'Neill, D. Menon, *Immunometabolism* **2017**, *38*, 395.
[54] C. Poiraud, G. Quereux, A. Knol, R. Allix, A. Khammari, B. Dreno, *Exp. Dermatol.* **2012**, *21*, 347.
[55] J. H. Laity, B. M. Lee, P. E. Wright, *Curr. Opin. Struct. Biol.* **2001**, *11*, 39.
[56] B. N. Okine, J. C. Gaspar, D. P. Finn, *Br. J. Pharmacol.* **2019**, *176*, 1421.
[57] Y. Shi, Y. Zou, Z. Shen, Y. Xiong, W. Zhang, C. Liu, S. Chen, *Int. J. Mol. Sci.* **2020**, *21*, 2612.
[58] C. Pauli, R. Whiteside, F. L. Heras, D. Nesic, J. Koziol, S. P. Grogan, J. Matyas, K. P. H. Pritzker, D. D. D'Lima, M. K. Lotz, *Osteoarthritis Cartilage* **2012**, *20*, 476.
[59] Y. Zou, Q. Li, D. Liu, J. Li, Q. Cai, C. Li, Q. Zhao, W. Xu, *Sci. Re* **2017**, *7*, 2454.